IEEE Access
Multidisciplinary | Rapid Review | Open Access Journal

Received 13 June 2023, accepted 27 June 2023, date of publication 3 July 2023, date of current version 7 July 2023.

*Digital Object Identifier 10.1109/ACCESS.2023.3291611*

RESEARCH ARTICLE

# Forward-Looking MIMO-SAR for Enhanced Radar Imaging in Autonomous Mobile Robots

**ADNAN ALBABA[1,2], MARC BAUDUIN[1], TIM VERBELEN[3], HICHEM SAHLI[1,2], AND ANDRÉ BOURDOUX[1], (Senior Member, IEEE)**

[1]Advanced RF Program, IMEC, 3001 Leuven, Belgium
[2]ETRO, Departement of Electronics and Informatics, Vrije Universiteit Brussel, 1050 Ixelles, Belgium
[3]IDLab, Department of Information Technology, Ghent University, 9052 Gent, Belgium

Corresponding author: Adnan Albaba (adnan.albaba@imec.be)

**ABSTRACT** Synthetic aperture radar (SAR) techniques are commonly used in spaceborne and airborne side-looking radar imaging applications, where the relatively high platform speeds enable the formation of very long synthetic apertures, which provide images with high angular resolution. However, the recent development of new autonomous ground vehicles, with relatively slow speeds, calls for new SAR imaging methods to obtain high angular resolution images. In this paper, the concept of forward-looking multiple-input multiple-output SAR (FL-MIMO-SAR) is analyzed and applied for short-range millimeter-wave radar forward-looking imaging in autonomous mobile robots (AMRs). Moreover, if the antenna inter-element spacing in the MIMO array is small, the FL-MIMO-SAR imaging system will provide low or no angular resolution refinement at the radar boresight region, i.e., Doppler beam sharpening (DBS) ineffective region. To solve that, the combination of FL-MIMO-SAR and sparse MIMO arrays with large inter-element spacing (FL-sparseMIMO-SAR) is proposed. Aspects such as the signal model, image reconstruction, complexity reduction, and the left-right ambiguity for FL-MIMO-SAR imaging systems are addressed. In addition, different imaging scenarios for AMRs are simulated using a frequency-modulated continuous wave radar simulator. Simulation results are validated with real measurements. It is shown that the proposed combination of FL-MIMO-SAR and MIMO arrays with large inter-element spacing manages to significantly suppress the grating lobes, which come from the sparsity in the antenna array. Moreover, the proposed FL-sparseMIMO-SAR helps to relax the requirements on the synthetic aperture length and solves the DBS-blind region problem, thanks to the larger real sparse MIMO array and the grating lobes suppression with the FL-SAR processing. Finally, the results show high potential for radar imaging systems, with FL-sparseMIMO-SAR capabilities, to be employed in the applications of AMRs towards smart factories and warehouses.

**INDEX TERMS** Autonomous mobile robots, radar imaging, FL-SAR, DBS, synthetic aperture radar, angular resolution, MIMO, complexity reduction, backprojection, image reconstruction, sparse antenna arrays, grating lobes suppression.

## I. INTRODUCTION

The use of millimeter-wave (mmW) radars as imaging sensors in autonomous platforms has seen a significant increase in the past two decades toward achieving full autonomy. For example, mmW radar imaging is used for automotive applications [1], field robotics [2], rotor aircrafts [3], human-centered robotics [4], collaborative robotics [5], autonomous trolley vehicles [6], and unmanned aerial vehicle [7].

For radar imaging applications, high range, Doppler, and angular resolution are required [8]. To achieve better range resolution, frequency-modulated continuous-wave (FMCW) with large frequency bandwidth can be employed. Moreover, better Doppler resolution can be obtained by increasing the observation time and carrier frequency of the radar. But when it comes to angular resolution, vision-only methods (e.g., cameras, LIDARs) provide images with significantly higher

The associate editor coordinating the review of this manuscript and approving it for publication was John Xun Yang.

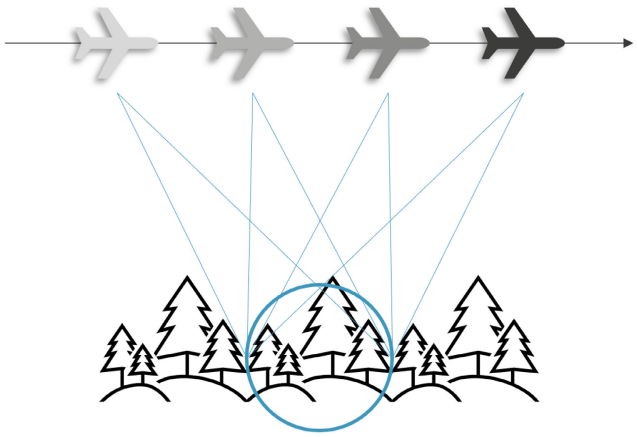

(a) Spotlight SAR is commonly used in spaceborne and airborne radar imaging applications with side-looking geometries.

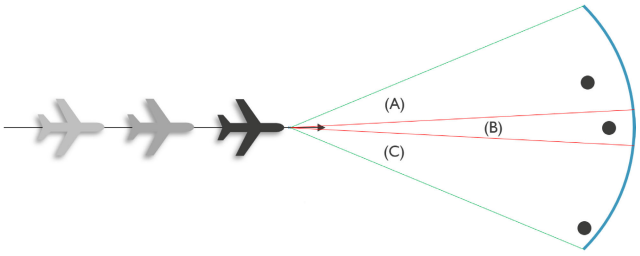


(b) The geometry of the FL-SAR. Applying DBS approaches for the target at the boresight in region (B) will be ineffective. Moreover, the angular resolution refinement for the target in region (C) will be higher than the one in region (A) due to the higher look angle.

**FIGURE 1. A comparison between side-looking and forward-looking SAR geometries.**

angular resolution than conventional radar-based images. However, the vision-only methods perform poorly in low visibility conditions. On the other hand, radars are capable of operating under challenging visual conditions such as darkness, smoke, and dust. Typically, higher radar angular resolution is achieved with larger antenna apertures (i.e., antenna arrays), which can be expensive or infeasible, especially in the case of ground-vehicles, where the size, weight, and price of the radar unit are severely limited.

To circumvent this issue, the concept of synthetic aperture radar (SAR) [9] can be used. SAR exploits the motion of the platform, on which the radar is mounted, by taking *snapshots* along the travel path. This enables the formation of large synthetic apertures with the collected snapshots, which can be used to achieve higher angular resolutions. SAR techniques have been applied in spaceborne and airborne radar imaging applications for decades [10]. Conventionally, side-looking SAR (SL-SAR), illustrated in Fig. 1a, is exploited in spaceborne and airborne radar imaging applications [10].

On the other hand, forward-looking SAR (FL-SAR), illustrated in Fig. 1b, has been applied in spaceborne-airborne bistatic SAR [11], [12], [13]. An early implementation of a radar system with FL-SAR capabilities is the DLR Radar-System SIREV [14], [15], which is an airborne radar with a fixed mounted antenna at the fuselage of an aircraft or a helicopter. Moreover, FL-SAR was employed for a gliding-down rotor aircraft, which forms a depression angle with respect to the scene center [3], [16].

In the case of FL-SAR, the geometry changes since the platform moves towards the imaged scene instead of passing alongside it, which is illustrated in Fig. 1a. For FL-SAR, it is possible to exploit the variations in the relative Doppler frequency shift of scatterers at different look angles with respect to the travel path of the platform. This approach is known as Doppler beam sharpening (DBS) [9], and it can provide refined angular resolutions. Fig. 1b illustrates the DBS concept. The radar echo of a point scatterer will have a specific Doppler frequency which depends on the scatterer relative radial speed. Since the speed of the platform, on which the radar is mounted, is known, the variations in the relative Doppler frequency shift of the point scatterer can be attributed to the cross-range deviation of the point scatterer, assuming that it is a static or cooperative moving target.

A drawback of the conventional DBS-based imaging approaches is that they provide no or poor angular resolution for look angles equal or close to zero degrees. For example, the use of DBS in region (B) in Fig. 1b will be ineffective due to the small look angle of the point scatterer. This is because a variation in angle in region (B) will only produce an insignificant Doppler shift variation. To solve this limitation, the combination of multiple input multiple output (MIMO) antenna arrays together with the concept of FL-SAR (FL-MIMO-SAR) is used [17]. In this case, the resulting angular resolution at the radar boresight will be the effective real aperture (i.e., MIMO array) angular resolution.

Recently, the techniques of spaceborne and airborne SAR have been adapted to be used in ground-vehicles for automotive applications. A typical automotive application for SL-SAR is parking assistance [18]. SL-SAR is also used for creating high resolution urban maps [19], [20]. In [21], a combination of forward-looking and side-looking radars on a car were exploited for ego-motion estimation and SL-SAR imaging, respectively.

However, the use of mmW radars, in the case of FL-MIMO-SAR for *slow* ground-vehicles, increases the sensitivity for positioning errors (i.e., millimeter-level accuracy is required). This results in relatively shorter synthetic apertures. Therefore, the angular resolution refinement, obtained by the FL-MIMO-SAR, is not only a result of the synthetic aperture but also the MIMO virtual aperture. A waveform-agnostic mathematical expression, which can be used to calculate the resulting refined angular resolution for a specific FL-MIMO-SAR system, was derived in [22]. Moreover, the mathematical expression in [22] can be used in the case of targets with look angles equal or close to zero degrees, where the angular resolution refinement is provided by the MIMO virtual aperture.

Examples of *slow* autonomous ground-vehicles are the autonomous guided vehicles (AGVs) [23] and the autonomous mobile robots (AMRs) [24], [25], which are

mainly used in smart factories and warehouses (also known as Industry 4.0). Unlike their predecessors, AGVs which rely on predefined tracks, AMRs are expected to navigate their way in constantly changing environments without misbehaving in the case of unexpected events or anomalies. Moreover, AMRs can perform a wide range of tasks such as object detection [26], collision avoidance [27], detection of spilled liquid [28], and terrain and environmental mapping [29].

For that to be achieved, a high degree of situational awareness is required and is enabled with a suite of sensors (mostly LIDARs and cameras), onboard the AMR, that allow continuous perception of the surroundings. Furthermore, the use of mmW radars together with other sensors (i.e., sensor fusion) in AMRs has been reported. For example, the use of radars with laser sensors (i.e., laser-radar) for accurate navigation was proposed in [30]. Moreover, the use of ultrasonic sensors and FMCW radars was proposed in [31] for obstacle detection. As for utilizing SAR techniques in AMRs, SL-SAR, using an ultra wideband radar, was exploited for constructing floor plans through smoke in [32] and for negative obstacle sensing in [33]. SL-SAR was also used for localizing passive ultrahigh-frequency radio frequency identification tags from a moving antenna carried on an AMR [34].

However, and to the best of the authors' knowledge, FL-SAR was not previously proposed for AMRs applications. For that to be enabled, shorter synthetic apertures are required due to the limitations that are imposed on the *slow* ground-vehicles. Moreover, such short apertures will lead to SAR images with low angular resolution which can be critical, especially for targets at the radar boresight (i.e., DBS-blind).

FL-SAR was used for automotive radar imaging, by utilizing a forward-scanning radar [35], [36]. Nevertheless, forward-scanning radars can be too expensive, especially for small autonomous ground-vehicles which are highly resource-limited. Moreover, the vehicle must remain stationary at each snapshot position for the scan duration. The applications of DBS, combined with MIMO beamforming, were demonstrated for better sensing of a vehicle surrounding environment [37]. But the angular resolution at the radar boresight will still be limited by the real MIMO angular resolution. In [38], the authors argue that FL-MIMO-SAR remains the best solution for targets in the DBS-blind regions. However, as mentioned earlier, the resulting angular resolution at the radar's boresight will be limited by the size of the effective real aperture. The work in [39] proposed to simplify the image reconstruction by ignoring the phase curvature and range migration compensation steps. But such simplification results in a loss of image quality. The work in [40] used a time-division multiplexing FL-MIMO-SAR with a random antenna activation pattern to account for the space-Doppler frequency coupling, which can be problematic for vehicles with high speeds. The Range–Doppler-based image reconstruction algorithm (RDA) was used in automotive SAR scenarios with good results for uniform linear trajectories [41]. Still, the RDA assumes a uniformly distributed grid of acquisition points across a linear path. In [42], the use of sensor fusion techniques was investigated towards enabling automotive SAR with nonuniform trajectories. Nonetheless, the current limitations on the accuracy of the available positioning sensors require an added SAR autofocusing step to provide high-quality automotive SAR images [43]. The work in [44] discussed the use of accurate motion compensation and the CLEAN algorithm [45] for removing the grating lobes that come from the nonuniform acquisition of snapshots along the SAR trajectory (i.e., sparsity in the synthetic aperture but not in the real MIMO aperture). However, on top of the added complexity due to applying the CLEAN algorithm, long synthetic apertures are still required to produce high resolution SAR images, especially for targets in the DBS-blind region.

In this paper, a combination of FL-MIMO-SAR and sparse MIMO arrays (FL-sparseMIMO-SAR), with large inter-element spacing, is proposed to relax the requirement on the synthetic aperture length and to solve the problem of DBS-blind regions. The exact FMCW signal model for the FL-MIMO-SAR problem is presented. Moreover, the decimated backprojection (Dec-BP) method [17] is used to reduce the computational complexity of the FL-MIMO-SAR image reconstruction. Aspects like model assumptions, image reconstruction, complexity reduction, and the left-right ambiguity for FL-MIMO-SAR are addressed. In addition, the relation between the FL-sparseMIMO-SAR and the resulting attenuation of the corresponding grating lobes is quantitatively analyzed. Furthermore, a FMCW radar simulator is used to simulate different use cases for AMR-based radar imaging. Finally, simulation results are validated with real measurements using a commercial radar sensor. It is shown that the FL-SAR processing helps attenuate the grating lobes, produced by the sparse MIMO array, significantly. Moreover, the proposed FL-sparseMIMO-SAR helps to relax the requirements on the synthetic aperture length and solves the DBS-blind region problem, thanks to the larger real sparse MIMO array and the grating lobes suppression with the FL-SAR processing. These results show high potential for radar imaging systems, with FL-MIMO-SAR capabilities, to be employed in the applications of AMRs towards smart factories and warehouses.

The rest of the paper is organized as follows: section II sets up the geometry as well as the FMCW signal model of the FL-MIMO-SAR problem. In section III, the combination of FL-MIMO-SAR with sparse MIMO arrays as well as the relation between different design parameters and the suppression of the resulting grating lobes are investigated. Simulation results are presented and discussed in section IV. In addition, section V presents and discusses the real measurement setup and results. Finally, the conclusions are drawn in section VI.

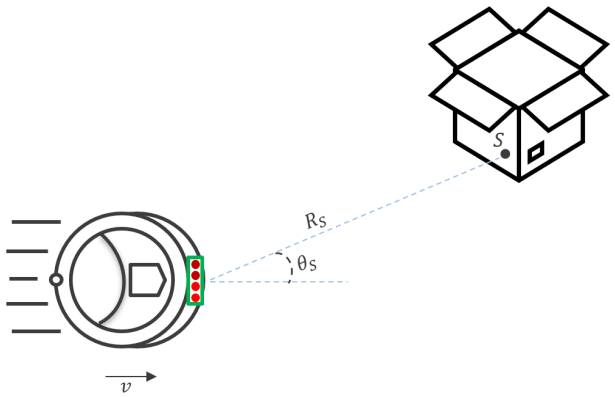


(a) An AMR, with a MIMO radar onboard, is moving forward. The forward motion enables the formation of high angular resolution FL-MIMO-SAR images.

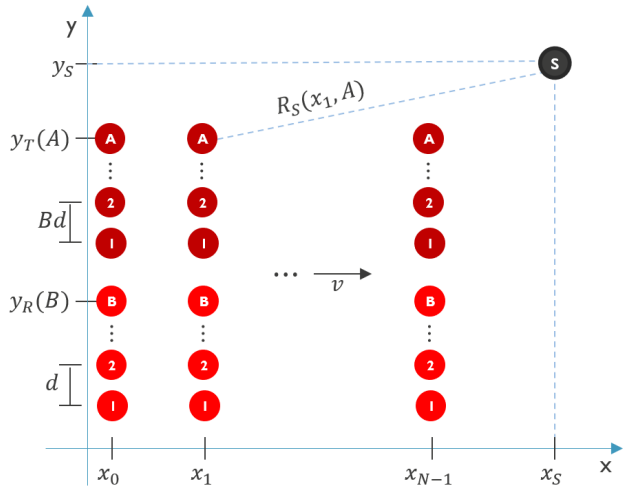


(b) The geometry of the 2-D FL-MIMO-SAR problem. The dark-red circles indicate the transmitters, while the light-red circles indicate the receivers. The scatterer is indicated by the black circle. The rest of the parameters are explained in subsection II-A

**FIGURE 2.** The geometry of the FL-MIMO-SAR problem.

## II. MODELLING

Fig. 2a illustrates a case scenario for the FL-MIMO-SAR problem. An AMR with a radar sensor unit, mounted in a forward-looking fashion, is moving. A box is in front of the AMR but slightly displaced in cross-range. For an arbitrary point $S$ on the box, $\theta_S$ denotes the look angle of $S$ with respect to the boresight of the radar. $R_S$ denotes the distance between the radar and the point $S$. Next, the detailed 2-D geometry and signal model of the FL-MIMO-SAR problem are explained.

### A. GEOMETRY AND SIGNAL MODEL

Fig. 2b illustrates, in more detail, the 2-D geometry for the FL-MIMO-SAR problem. The $x$-axis denotes the down-range and the $y$-axis denotes the cross-range. The dark-red circles indicate the transmitters at the snapshot positions, whereas the light-red circles indicate the receivers at the snapshot positions. The point scatterer $S$ at $\{x_s, y_S\}$ is indicated by the black circle, which is assumed to be static. The platform, on which the radar is mounted, is moving towards the scatterer $S$ with a velocity $v = \sqrt{\dot{x}^2 + \dot{y}^2}$, which is assumed to be constant. $x_0$, $x_1$, and $x_{N-1}$ denote the x-coordinates of the radar first, second, and $N$th snapshot, respectively, where $n = 0, 1, \ldots, N-1$ is the chirp index (i.e., slow time/snapshot).

For what follows, we consider a generic 1-D time-division multiplexing (TDM) MIMO FMCW radar, placed on the $y$-axis as illustrated in Fig. 2b. The MIMO array consists of $A$ transmitters $T_a$ ($a = 1, 2, \ldots, A$) and $B$ receivers $R_b$ ($b = 1, 2, \ldots, B$) with spacing $d$ between two receivers, and $Bd$ between two transmitters. The resulting virtual array consists of $A \times B$ antennas with spacing $d$ between two virtual antennas. $y_T(a)$ and $y_R(b)$ denote the cross-range positions of transmitter $a$ and receiver $b$, respectively. $R_S(x_1, A)$ denotes the distance of $S$ from transmitter $A$ at position $x_1$.

We also consider the following FMCW radar parameters:

$$\lambda = \frac{c}{f_c}, \quad T_p = T_c + T_i + T_r, \quad \alpha = \frac{BW}{T_c}$$

where $\lambda$ is the wavelength, $c$ is the speed of light, $f_c$ is the start frequency of the chirp, $T_p$ is the chirp repetition interval, $T_c$ is the chirp duration, $T_i$ is the chirp idle time, $T_r$ is the chirp return time, $\alpha$ is the chirp slope, and $BW$ is the bandwidth. We also define $t_f \in [0 : T_c]$ to be the intra-chirp time (fast time) and $f_s$ to be the baseband ADC sampling frequency. Moreover, a given transmitter $T_a$ in TDM-MIMO is active at the slow-time instants $(An + a)T_p$.

Following these definitions, the distance traveled by transmitters and receivers at $(a, b, n, t_f)$ is equal to $(x_0 + AnvT_p + avT_p + vt_f)$. For simplicity, we assume $x_0 = 0$ which denotes the initial $x$-coordinate of all transmitters and receivers, see Fig. 2b. The two-way range at $(a, b, n, t_f)$ is then expressed as:

$$\begin{aligned}\mathcal{R}(a, b, n, t_f) &= \sqrt{(x_s - AnvT_p - avT_p - vt_f)^2 + (y_s - y_R(b))^2} \\ &\quad + \sqrt{(x_s - AnvT_p - avT_p - vt_f)^2 + (y_S - y_T(a))^2} \end{aligned} \tag{1}$$

and the two way propagation delay $\tau$ at $(a, b, n, t_f)$ is given by

$$\tau(a, b, n, t_f) = \frac{\mathcal{R}(a, b, n, t_f)}{c} \tag{2}$$

The transmitted up-chirp signal can be expressed as

$$s(t_f) = e^{i\pi\alpha t_f^2} e^{i2\pi f_c t_f} \tag{3}$$

The radar receives the echo from the scatterer after a propagation delay $\tau$, and the received signal can be expressed as

$$\begin{aligned} r(a, b, n, t_f) = \Lambda e^{i\pi\alpha t_f^2} e^{i\pi\alpha\tau(a,b,n,t_f)^2} \\ e^{-i2\pi\alpha t_f \tau(a,b,n,t_f)} e^{i2\pi f_c t_f} e^{-i2\pi f_c \tau(a,b,n,t_f)} \end{aligned} \tag{4}$$

where $\Lambda$ is a complex amplitude term. For de-chirping, the received signal is multiplied by the complex conjugate of the transmitted signal. After de-chirping, the baseband beat frequency signal is obtained and can be expressed as:

$$\zeta(a,b,n,k) = \Lambda e^{-i2\pi f_c \tau(a,b,n,\frac{k}{f_s})} e^{-i2\pi\alpha\frac{k}{f_s}\tau(a,b,n,\frac{k}{f_s})} e^{i\pi\alpha\tau(a,b,n,\frac{k}{f_s})^2} \quad (5)$$

where $\frac{k}{f_s}$ $(k = 0, 1, \ldots, K-1)$ are the sampling instants.

### B. MODEL ASSUMPTIONS AND APPROXIMATIONS

In the above-described signal model (see subsection II-A), the targets are assumed to be isotropic point scatterers. For realistic complex scenes, with many targets, the total reflected field will contain the incident field as well as the scattered field (i.e., local scattering between the point targets). This will make the equations intractable except for very simple geometries. To make the problem more tractable, the scattered field is assumed to be much weaker than the incident field and is therefore ignored. Such approximation is known as the ''first Born approximation''. Simulations made with this approximation will not reproduce multipath artifacts that are observed in real measurements [46].

Another important assumption, made in subsection II-A, is that the targets are static. In SAR, compressing the cross-range data (i.e., target focusing) requires precise compensation of the targets' motion information [47]. Accordingly, the imaged scene is assumed to be stationary in SAR methods. The presence of a dynamic target results in smearing artifacts in the reconstructed SAR image [47]. It also leads to moving targets being reconstructed at the wrong positions. However, for the case of AMRs in smart warehouses, it is acceptable to assume a stationary scene, given the nature of the scene (i.e., mostly stationary in a fully automated warehouse).

It is important to mention that perfect knowledge of the ego-positions and ego-velocity at every snapshot position is assumed, which is only achievable in computer simulations. For real case scenarios, the information on the positioning and the velocity of the platform is obtained using a suite of sensors (e.g., GNSS/GPS for ego-positioning and odometer for ego-velocity), which will be contaminated with sensing errors. Due to the use of mmW radar, positioning and odometry sensors with millimeter-level accuracy are required. Similar to the case of moving targets' miss-compensation, failing to accurately compensate ego-positions and ego-velocity information leads to undesirable effects on the reconstructed SAR image [47]. Smearing artifacts as well as splitting in the mainlobe are reported as direct results of positioning errors in automotive SL-SAR images [48]. Moreover, the severity of these artifacts increases for targets at wide look angles (i.e., more severe for targets in forward-looking positions) [48]. Thus, smearing and splitting artifacts are expected for FL-MIMO-SAR images with ego-positions and ego-velocity errors.

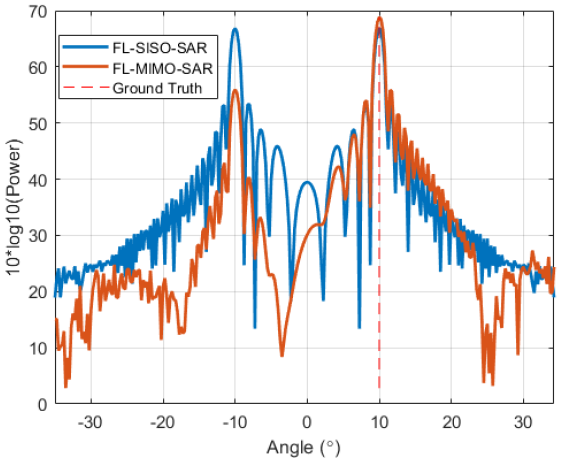


**FIGURE 3.** The MIMO array topology in the FL-MIMO-SAR attenuates the mirrored ghost target.

Last but not least, given the forward-looking geometry, targets that are symmetrical around the 0° look angle correspond to the same slant range history. This symmetry leads to a left-right ambiguity around the radar boresight. Therefore, the FL-SISO-SAR-based approaches cannot discriminate between positive and negative angles, resulting in a mirroring effect around 0°. However, contrary to the case of FL-SISO-SAR, where the left-right ambiguity problem is maximized, the MIMO array topology in the case of FL-MIMO-SAR helps to attenuate the mirrors to a certain level, thanks to the differences in the geometrical relations between the mirror and each transmitter-receiver pair in the array. Fig. 3 illustrates the effect of a $2 \times 4$ MIMO array with FL-MIMO-SAR on the left-right ambiguity. In this work, and since it is out of our scope, we only rely on the attenuation that is provided by the MIMO array topology.

### C. IMAGE RECONSTRUCTION AND COMPLEXITY REDUCTION

To reconstruct the FL-MIMO-SAR image with an optimal signal-to-noise ratio (SNR), the matched filter (MF) solution is derived as follows:

$$Z_{\mathrm{MF}}(l,m) = \sum_{a=0}^{A-1}\sum_{b=0}^{B-1}\sum_{n=0}^{N-1}\sum_{k=0}^{K-1} \zeta(a,b,n,k)\gamma(a,b,n,k,l,m) \quad (6)$$

Moreover, $l = \frac{2x_s BW}{c}$ and $m$ are the range and cross-range bin indices, respectively. $\gamma(a,b,n,k,l,m)$ is the complex conjugate of the hypothetical beat frequency signal $\zeta(a,b,n,k,l,m)$. It is clear that the computational complexity of the solution in (6) makes it hard to be implemented in real-time. The four dimensional summation over $A$, $B$, $K$, and $N$ must be computed for all values of $l = 0, 1, \ldots, L-1$ and $m = 0, 1, \ldots, M-1$, resulting in a complexity of $\mathcal{O}(LMNKAB)$, hence, a complexity reduction is needed.

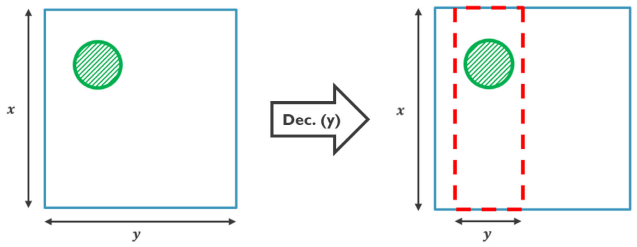


**FIGURE 4.** The decimation in the slow-time samples is equivalent to reducing the field of view in the cross-range (here, *y*-axis). This is due to the formation of aliasing ghosts outside the unambiguous field-of-view in cross-range (marked by the red dashed rectangle) as a result to the decimation.

One way to reduce the computational complexity of (6) is to apply the Fourier transform on the fast-time samples to get the range profiles, which is done in the backprojection (BP) method [49]. The BP reconstructed 2-D image $Z_{\text{BP}}(l, m)$ is then derived as:

$$Z_{\text{BP}}(l, m) = \sum_{a=0}^{A-1} \sum_{b=0}^{B-1} \sum_{n=0}^{N-1} \mathcal{F}_k\{\zeta(a, b, n, k)\} e^{\frac{i2\pi f_c \tilde{\mathcal{R}}(a,b,n,l,m)}{c}} \quad (7)$$

where $\mathcal{F}_k$ denotes the 1-D Fourier transform over the fast-time samples, and $\tilde{\mathcal{R}}$ is an approximated version of $\mathcal{R}$ by ignoring the intra-chirp variations. An interpolation step is then needed to map $\tilde{\mathcal{R}}$ into the range profile (constructed by $\mathcal{F}_k$). Thanks to the fast implementation of the Fourier transform, the computational complexity of (7) is reduced but still relatively high.

To further reduce the computational complexity of (7), slow-time decimation can be applied, which is done in the Dec-BP method [17]. Fig. 4 illustrates the slow-time decimation process. To avoid aliasing and SNR loss, due to decimation, a digital low-pass filter (LPF) is implemented and the finite impulse response LPF is applied to the slow-time sample set prior to the decimation. This allows for reconstructing within a reduced alias-free down-sampled field of view (FOV). The Dec-BP reconstructed 2-D image $Z_{\text{DBP}}(l, m)$ is then derived as:

$$Z_{\text{DBP}}(l, m) = \sum_{a=0}^{A-1} \sum_{b=0}^{B-1} \sum_{n=0}^{\hat{N}-1} \mathcal{F}_k\{\bar{\zeta}(a, b, n, k)\} e^{\frac{i2\pi f_c \tilde{\mathcal{R}}(a,b,n\beta,l,m)}{c}} \quad (8)$$

where $\bar{\zeta}$ is the low-pass filtered and decimated beat frequency, $\hat{N} = \frac{N}{\beta}$ is the decimated version of $N$, and the decimation factor $\beta$ is obtained as follows:

$$\beta = \left\lfloor \frac{N\lambda}{2vT_{\text{cpi}} \arctan\left(\max(\theta_S)\right)} \right\rfloor \quad (9)$$

where, $T_{\text{cpi}} = ANT_p$ denotes the coherent processing interval (CPI) and $\max(\theta_S)$ denotes the maximum reconstructed angle bin. Applying Dec-BP for the FL-MIMO-SAR case results in a reduced complexity with limited FoV (depending on $\beta$) but without sacrificing angular resolution.

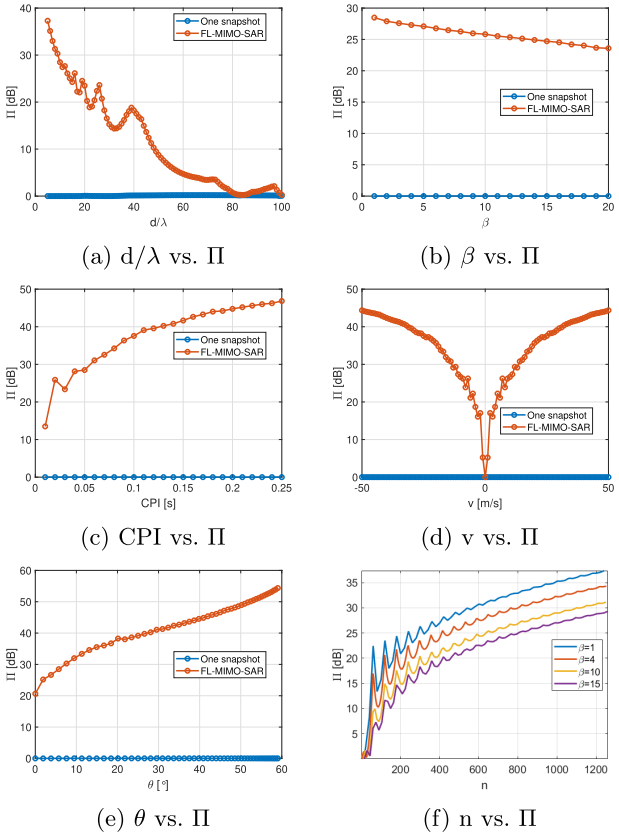


(a) d/$\lambda$ vs. $\Pi$ (b) $\beta$ vs. $\Pi$

(c) CPI vs. $\Pi$ (d) v vs. $\Pi$

(e) $\theta$ vs. $\Pi$ (f) n vs. $\Pi$

**FIGURE 5.** Effects of the choice of different parameters (*d*, $\beta$, CPI, *v*, $\theta$, and *n*) on the grating lobe suppression performance $\Pi$.

It is worth noting that more complexity reduction methods were reported in the literature. For example, reducing the number of reconstruction points by considering a Polar-grid-based BP can be used for SL-SAR applications. However, going from a Cartesian to a Polar-grid-based BP is not a straightforward procedure for FL-SAR geometries (unlike in SL-SAR), and a 2-D interpolation step is needed which also adds to the overall complexity. In addition, the Fast-Factorized BP was reported in [50] for reducing the computational complexity of the SAR image reconstruction. However, this reduction comes at the cost of angular resolution.

In this work, we opted for the Dec-BP method as it does not affect the image quality but reduces the maximum alias-free FoV. Thanks to the nature of the application (i.e., indoor short-range AMR imaging), the required reconstructed FoV is reduced to $\pm 35°$, which enables the use of the Dec-BP method.

## III. FL-MIMO-SAR WITH SPARSE MIMO ARRAYS

As mentioned in section I, higher radar angular resolution can be achieved with larger apertures. Typically, radar apertures are populated with antennas, with sufficient inter-element

**TABLE 1. Design parameters in all simulation scenarios: target (range, angle) positions and their respective amplitudes Λ.**

| Scenario | Target 1 | Λ | Target 2 | Λ | Target 3 | Λ |
|---|---|---|---|---|---|---|
| 1 | (5.75m , 0°) | 1dB | - | - | - | - |
| 2 | (6.5m , 6°) | 1dB | (6.5m , -6°) | 1dB | - | - |
| 3 | (4.85m , 8°) | 10dB | (5m , -13°) | 10dB | (6m , 0°) | 1.78dB |
| 4 | (8.51m , -0.8°) | 1dB | - | - | - | - |

spacing, to ensure alias-free imaging. However, this approach can be expensive or infeasible, especially in the case of AMRs, where resources such as the weight and price of the radar unit are highly limited.

By increasing the inter-element spacing, it is possible to create larger radar apertures without the need for adding more antenna elements. This shall reduce the price and system complexity while providing a higher angular resolution that corresponds to the aperture size. However, the large inter-spacing between antennas (i.e., larger than half wavelength) results in the formation of grating lobes.

A grating lobe can be identified as a spatial aliasing or a replica of the main lobe but in the wrong location. Although these grating lobes do not affect the effective resolution, they corrupt the quality of the image significantly and therefore must be suppressed. To determine the angles $\phi$ of the grating lobes for a target $S$ at angle $\theta_S$, the following formula is used:

$$\phi(g) = \arcsin\left(\frac{g2\pi + \sin(\theta_S)\frac{2\pi d}{\lambda}}{2\pi} \times \frac{\lambda}{d}\right) \tag{10}$$

where $d$ denotes the spacing between two elements in the array, $g = \pm 1, \pm 2, \ldots, \pm G - 1$ is the grating lobe index, and $G = \frac{2d}{\lambda}$ is an integer, keeping only the acceptable (i.e. real) values in (10).

From equation (10), it can be seen that the location of a grating lobe $\phi$ is related to $\theta_S$, which depends on the spatial relation between the transmitter-receiver pair and the target. Therefore, and by combining FL-SAR with sparse MIMO arrays, large inter-element spacing, (FL-sparseMIMO-SAR), the resulting grating lobes are expected to be suppressed due to the fact that the Doppler phase history for a target is different from one virtual array element to another, and this difference becomes significant for large virtual antenna apertures.

To quantitatively analyze this behavior, the ratio between the power of the main lobe to the power of the grating lobe $\Pi$ is used. Since $\theta$ in (10) is function of $(a, b, n, k)$, it is possible to study the relation between $\Pi$ and other system design parameters given the following relation:

$$\Pi(a, b, n, k) = 10 \log\left(\frac{\left|Z_{\mathrm{BP}}\left(\theta(a, b, n, k)\right)\right|^2}{\left|Z_{\mathrm{BP}}\left(\phi(\theta(a, b, n, k), g)\right)\right|^2}\right) \tag{11}$$

where, in our case, $g = \pm 1$ (i.e., the nearest grating lobes).

Fig. 5 illustrates that, for the case of a large inter-element spaced MIMO radar, the grating lobes are not suppressed and have amplitudes approximately equal to the main lobe (i.e., $\Pi = 0$ dB) in the case of one snapshot. However, the FL-sparseMIMO-SAR shows good performance in suppressing the grating lobes (i.e. $\Pi > 0$ dB) depending on the choice of the parameters. Fig. 5a shows how $\Pi$ degrades when the inter-element spacing $d$ is increased. Moreover, for an increase in $\beta$ a small degradation in $\Pi$ is shown in Fig. 5b. On the other hand, Fig. 5c and Fig. 5d show how the grating lobe suppression improves for increasing $T_{\mathrm{cpi}}$ (at constant $v$) or increasing $v$ (at constant $N$), respectively. In addition, Fig. 5e shows improving $\Pi$ for increasing the target angle. Lastly, Fig. 5f illustrates the relation between the number of snapshots evaluated in the SAR processing, the decimation rate $\beta$, and the grating lobe suppression index $\Pi$. Not only it shows the inverse relation between $\beta$ and $\Pi$, but also shows that a trade-off between the number of snapshots to be considered for SAR (i.e., the length of the traveled path or length of the synthetic aperture or $T_{\mathrm{cpi}}$) and the desired level of grating lobe suppression can be applied towards reducing the SAR processing complexity.

In addition, the FL-sparseMIMO-SAR provides high angular resolution at the radar boresight, thanks to the large aperture, where the FL-MIMO-SAR is limited, see section I and Fig. 1b.

## IV. SIMULATION RESULTS

In this section, the results from the simulated scenarios are presented and discussed. Four different scenarios were simulated with an input SNR (i.e., SNR of the ADC raw data before any processing gain) of $10dB$ for all targets. The results for the first three simulation scenarios were produced using the following parameters: $f_c = 79$ GHz, $BW = 2$ GHz, $f_s = 6.25$ MHz, $v = 0.5$ m/s, $T_p = 800\ \mu s$, CPI $= 4$ s, and the total synthetic aperture length is 3 m. For the fourth simulation scenario, the following parameters were used: $f_c = 79$ GHz, $BW = 2.2$ GHz, $f_s = 6.25$ MHz, $v = 0.35$ m/s, $T_p = 60.9\ \mu s$, CPI $= 0.44$ s, and the total synthetic aperture length is 0.154 m. In the following simulation scenarios, we focus on the azimuth as the cross-range of interest. It is worth noting that no windowing or filtering was applied.

In the first three scenarios, the MIMO array used is a generic 1-D TDM-MIMO with two transmitters and four receivers. The resulting virtual array consists of 8 virtual antennas with spacing $\frac{\lambda}{2}$ between each two virtual antennas. In the fourth scenario, the sparse MIMO array used is a 1-D TDM-MIMO with two transmitters and four receivers. The resulting virtual array consists of 8 virtual antennas with spacing $5\lambda$ between every two virtual antennas.

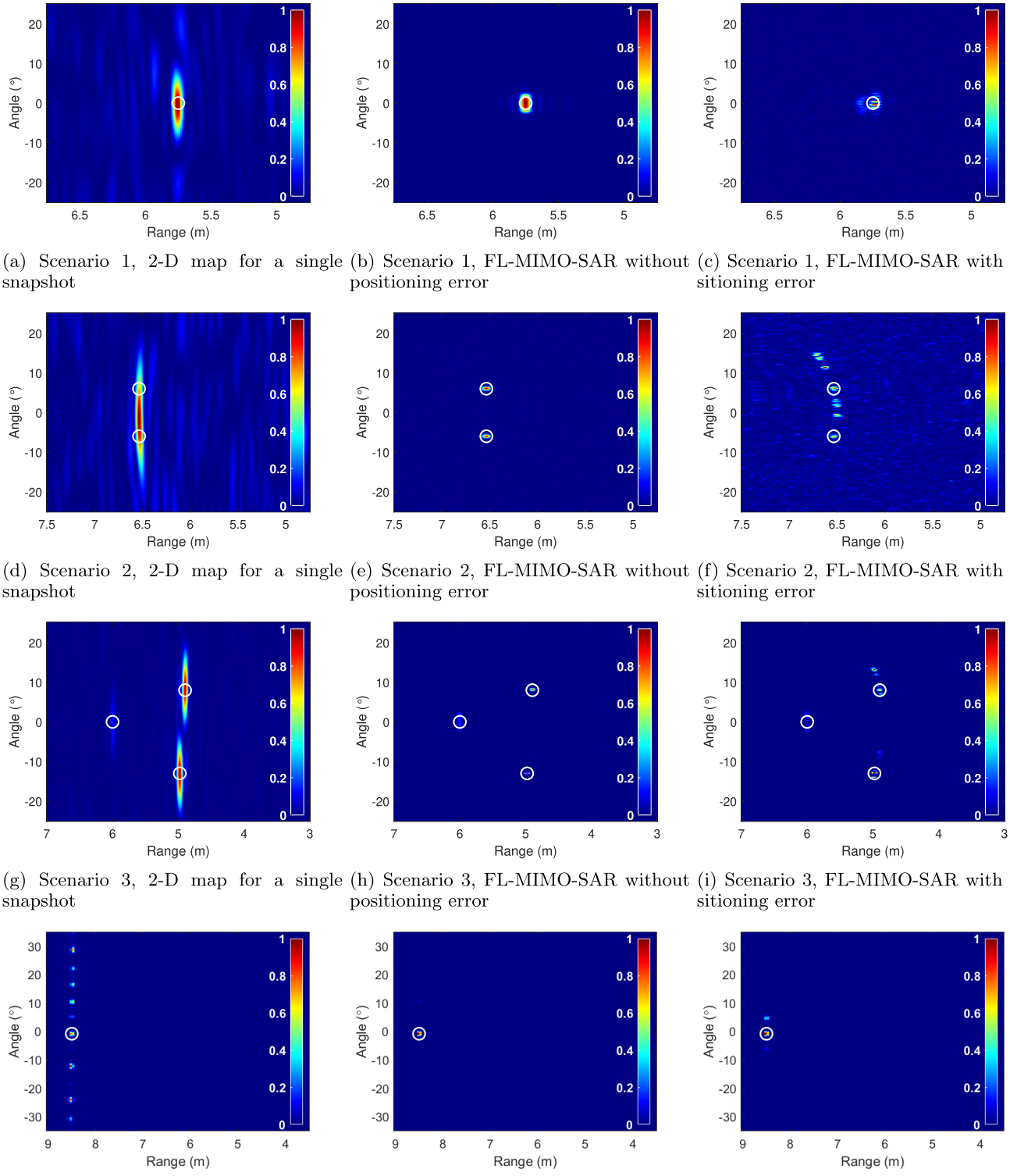


(a) Scenario 1, 2-D map for a single snapshot

(b) Scenario 1, FL-MIMO-SAR without positioning error

(c) Scenario 1, FL-MIMO-SAR with positioning error

(d) Scenario 2, 2-D map for a single snapshot

(e) Scenario 2, FL-MIMO-SAR without positioning error

(f) Scenario 2, FL-MIMO-SAR with positioning error

(g) Scenario 3, 2-D map for a single snapshot

(h) Scenario 3, FL-MIMO-SAR without positioning error

(i) Scenario 3, FL-MIMO-SAR with positioning error

(j) Scenario 4, 2-D map for a single snapshot

(k) Scenario 4, FL-sparseMIMO-SAR without positioning error

(l) Scenario 4, FL-sparseMIMO-SAR with positioning error

**FIGURE 6. Simulation results for scenario 1 (a-c), scenario 2 (d-f), scenario 3 (g-i), and scenario 4 (j-l). The white circles indicate the true target positions. All colorbars show normalized voltage scales.**

Table 1 shows the target configurations in each scenario. In scenarios 1 and 4, a single point target at the boresight is simulated. In scenario 2, two point targets, with similar amplitudes $\Lambda$, at opposite look angles and in the same range

**TABLE 2.** Target parameters (range $\mathcal{R}$, angle $\theta$) in all experimental scenarios.

| Scenario | Target 1 | Target 2 | Target 3 | Target 4 |
|---|---|---|---|---|
| 1 | $\mathcal{R}$:5.75m , $\theta$:0.2° | - | - | - |
| 2 | $\mathcal{R}$:6.5m , $\theta$:6° | $\mathcal{R}$:6.5m , $\theta$:-6° | - | - |
| 3 | $\mathcal{R}$:5.98m , $\theta$:0.3° | $\mathcal{R}$:4.85m , $\theta$:8.3° | $\mathcal{R}$:4.89m , $\theta$:-13.1° | - |
| 4 | $\mathcal{R}$:5.16m , $\theta$:3.2° | $\mathcal{R}$:5.16m , $\theta$:-3.4° | $\mathcal{R}$:5.76m , $\theta$:-3° | $\mathcal{R}$:5.75m , $\theta$:3° |
| 5 | $\mathcal{R}$:8.51m , $\theta$:-0.8° | - | - | - |

bin are simulated. In scenario 3, three point targets with different amplitudes $\Lambda$ are simulated at different positions. In addition, a random positioning error, in the range of millimeters and changing randomly at every snapshot, was added in all three scenarios to observe the effect of this type of non-ideality on the resulting FL-MIMO-SAR images.

For each scenario, the 2-D images of the single snapshot and the FL-MIMO-SAR, with and without positioning error, are illustrated in Fig. 6. The white circles on the 2-D maps indicate the ground truth. By comparing Fig. 6a, Fig. 6d, and Fig. 6g, which illustrate the 2-D maps for a single snapshot in the three scenarios, respectively, with Fig. 6b, Fig. 6e, and Fig. 6h, which illustrate the 2-D maps for the FL-MIMO-SAR without positioning error in the three scenarios, respectively, it is clear that the FL-MIMO-SAR approach produces high angular resolution. Moreover, it can be seen that the FL-MIMO-SAR results in a better SNR compared to the single snapshot case thanks to the coherent integration of all snapshots.

Moreover, the resulting angular resolution refinement for the target in scenario 1 (Fig. 6b) is less than the resulting angular resolution refinement for the targets in scenario 2 (Fig. 6e). This is due to the zero look angle of the target in scenario 1, which renders the DBS approach ineffective. As expected, artifacts such as splitting of the mainlobe as well as smearing are shown in Fig. 6c, Fig. 6f, and Fig. 6i, which illustrate the 2-D maps for the FL-MIMO-SAR with random positioning error in the three scenarios, respectively.

Furthermore, Fig. 6j illustrates 2-D map for a single snapshot in simulation scenario 4. Here, and opposite to the case of Fig. 6a, Fig. 6d, and Fig. 6g, the resulting angular resolution is higher due to the large real MIMO aperture (sparse MIMO array). However, the sub-wavelength inter-element spacing results in the formation of grating lobes, which corrupt the 2-D map in Fig. 6j. On the other hand, Fig. 6k and Fig. 6l, which illustrate the 2-D maps for the FL-sparseMIMO-SAR with and without positioning error, respectively, show the resulting suppression of the grating lobes to be significant.

## V. EXPERIMENTAL RESULTS

In this section, the equipment, experimental setup, and results using real measurements are presented and discussed.

### A. FL-MIMO-SAR EXPERIMENTAL SETUP

Here, the objective is to verify the simulation results (see section IV), which simulate several scenarios for AMR radar imaging applications. To do that, a low-cost, robot with open-source software (i.e., AMR) is used as the moving platform (see Fig. 7a). Moreover, a Texas Instruments AWR1243 mmW radar sensor is deployed onboard the AMR (see Fig. 7b). The radar sensor has four receivers and two transmit antennas (on the azimuth cross-range), similar to the topology shown in Fig. 2b. The following parameters are considered in the real measurements: $f_c = 79$ GHz, $BW = 2$ GHz, $f_s = 6.25$ MHz, $T_p = 800\ \mu s$, CPI $= 4$ s, and the total synthetic aperture length is 3 m. The AMR accelerates from $v = 0$ to 0.5 m/s. Poles, with corner reflectors, as well as a table, with metal legs, were used as targets (see Fig. 7c and Fig. 7d). The maximum unambiguous range is 21.06 m. The range resolution is 0.075 m. The maximum unambiguous velocity is 0.593 m/s. The velocity resolution is 0.0047 m/s. The real aperture angular resolution (at boresight) is 16.37°.

In addition, a motion capture (MOCAP) system is used to digitally record the movement of the AMR. This is an important step to ensure the accurate compensation of the AMR motion in order to achieve satisfactory results (see section IV for the effects of inaccurate motion compensation). However, the used MOCAP system has a frame rate of 14fps (due to some experimental setup limitations). Thus, interpolation is needed to estimate the velocity and position of the AMR along its trajectory. This results in an error in the range of centimeters-to-millimeters in the positioning information. Moreover, the yaw of the radar shifts gradually along the trajectory as the AMR slightly shifts its trajectory while accelerating due to vibrations.

Four different experimental scenarios (1-4) are performed using this FL-MIMO-SAR setup. In scenario 1, a pole, with a corner reflector, is used as a target at the boresight (see Fig. 8a). In scenario 2, two poles, each with a corner reflector, are used as targets at opposite look angles (see Fig. 8c). In scenario 3, three poles, two with a corner reflector and one without, are used as targets at different positions (see Fig. 8e). In scenario 4, a table, with four metal legs, is used as a complex target (see Fig. 8g). Table 2 shows the number of targets and their positions in each experimental scenario.

### B. FL-sparseMIMO-SAR EXPERIMENTAL SETUP

Similar to the FL-MIMO-SAR setup, an AMR is used as the moving platform (see Fig. 9a). Moreover, a Texas Instruments AWR2243 cascaded mmW radar sensor is deployed onboard the AMR (see Fig. 9a). The following parameters are considered in the real measurements: $f_c = 79$ GHz, $BW = 2.2$ GHz, $f_s = 6.25$ MHz, $T_p = 60.9\ \mu s$, CPI $= 0.44$ s,

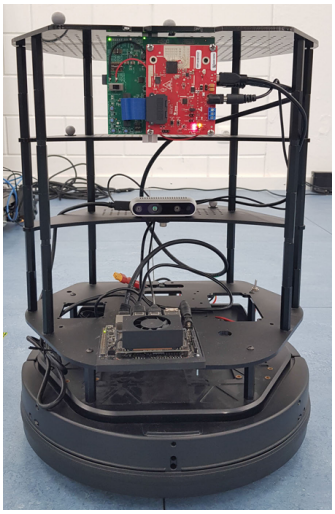

(a) The AMR with the radar

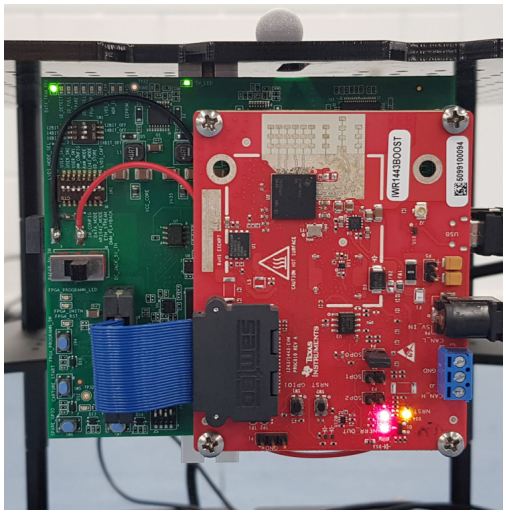


(b) The radar sensor unit

(c) A point-of-view shot for scenario 1

(d) A side-view shot for scenario 4

**FIGURE 7.** **The experimental setup for the real measurements.**

and the total synthetic aperture length is 0.154 m. The AMR accelerates from $v = 0$ to 0.35 m/s. The maximum unambiguous range is 23.38 m. The range resolution is 0.075 m. The maximum unambiguous velocity is 18.97 m/s. The velocity resolution is 0.13 m/s. The real aperture angular resolution (at boresight) is 1.35°. A corner reflector was used as a target in experimental scenario 5, see Table 2.

The cascaded radar sensor has 16 receivers and 12 transmit antennas (9 on the azimuth cross-range and 3 elevation cross-range). Since, in this work, the azimuth cross-range is the cross-range of interest, the number of effective transmit antennas is 9. Together with the 16 receivers, a uniform linear virtual array of 144 channels is formed. After eliminating the overlapping ones, the effective uniform linear virtual array

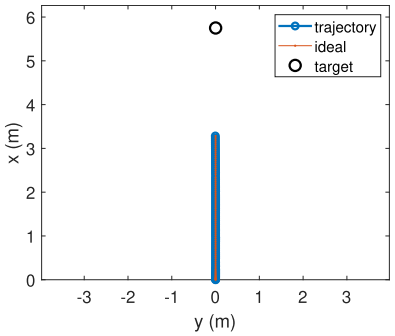


(a) The geometry of scenario 1

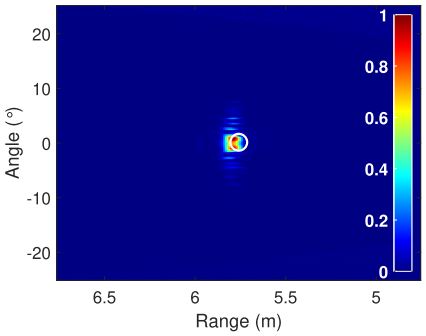


(b) The resulting image for scenario 1

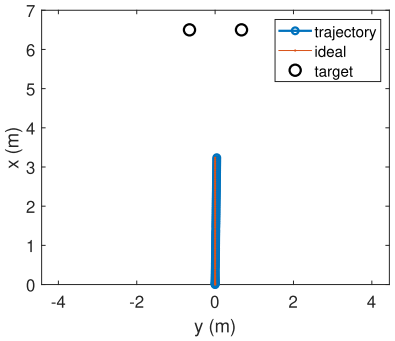


(c) The geometry of scenario 2

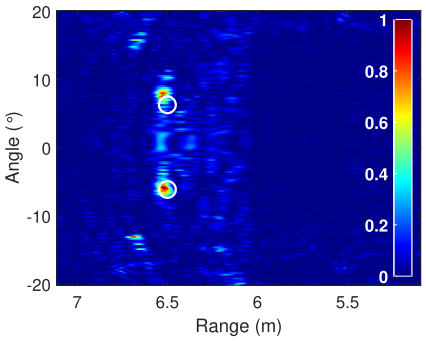


(d) The resulting image for scenario 2

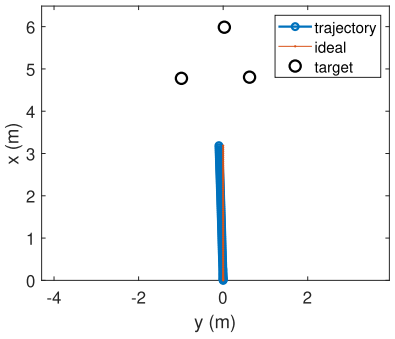


(e) The geometry of scenario 3

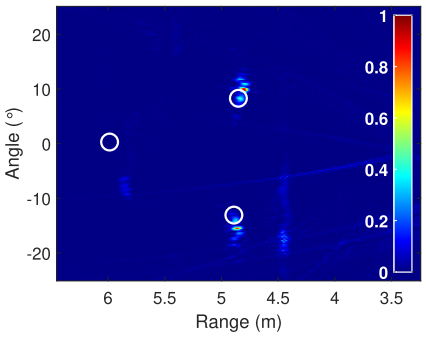


(f) The resulting image for scenario 3

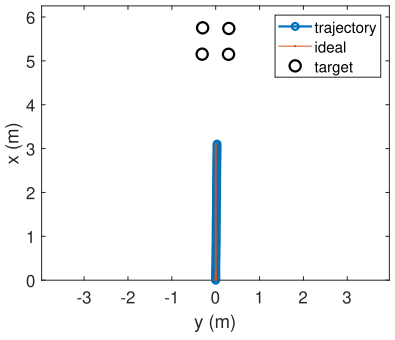


(g) The geometry of scenario 4

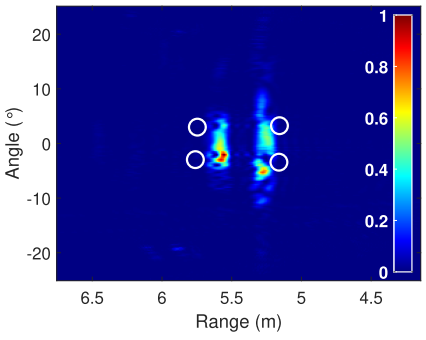


(h) The resulting image for scenario 4

**FIGURE 8.** **The 2-D geometry and the corresponding 2-D FL-MIMO-SAR images are shown for the first four different experimental scenarios. The circles (white or black) indicate the true target positions. All colorbars show normalized voltage scales.**

consists of 86 channels with an inter-element spacing of $\frac{\lambda}{2}$. However, and to utilize a sparse MIMO array, only 9 (out of 86) channels are used to form the FL-sparseMIMO-SAR 2-D images. This topology results in a sparse uniform linear

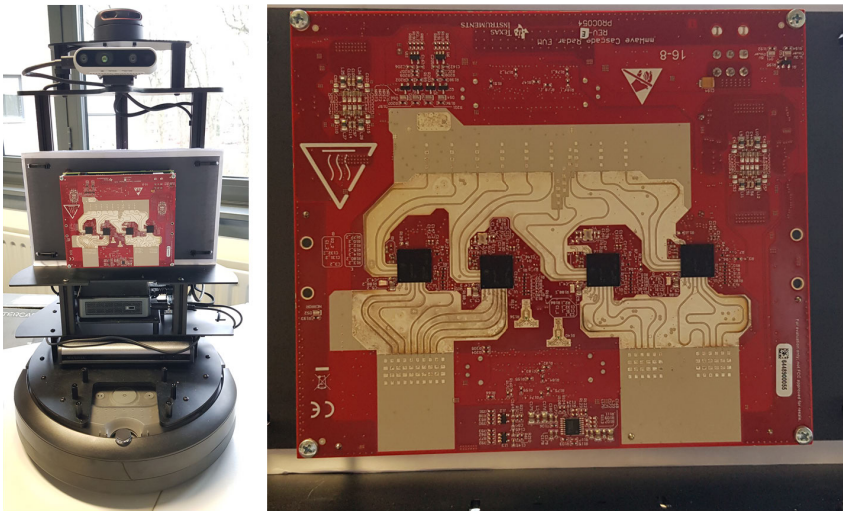

(a) The AMR with the cascaded radar

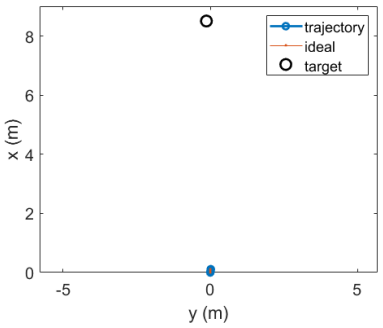


(b) The geometry of scenario 5

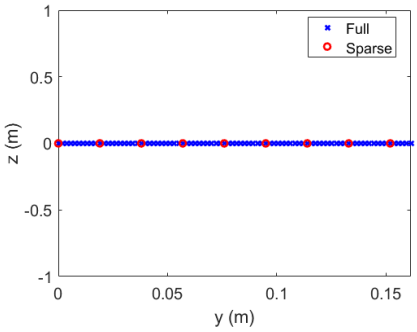


(c) The resulting full/sparse virtual array

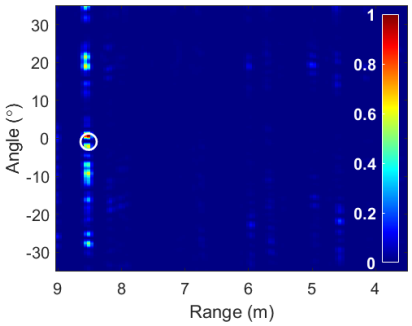


(d) The resulting image for scenario 5 (single snapshot)

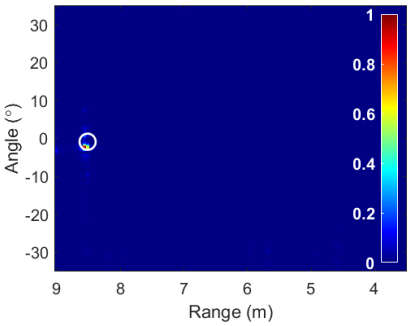


(e) The resulting image for scenario 5 (FL-sparseMIMO-SAR)

**FIGURE 9. The experimental setup, geometry, virtual antenna array topology, and the resulting 2-D images are shown for the fifth experimental scenario with the cascaded radar. The circles (white or black) indicate the true target positions. All colorbars show normalized voltage scales.**

virtual array that consists of 9 channels with an inter-element spacing of 5λ, see Fig. 9c.

Unlike in the FL-MIMO-SAR experimental scenarios 1-4, an Inertial Measurement Unit (IMU) sensor, onboard the AMR, is used to digitally record the movement of the AMR. The update rate of the IMU sensor is 11 Hz. Thus, interpolation is needed to estimate the velocity and position of the AMR along its trajectory. On the other hand, the gradual shift in yaw of the radar along the trajectory is recorded by the IMU as the AMR slightly shifts its trajectory while accelerating due to vibrations. Overall, an error in the range of centimeters-to-millimeters in the positioning information is produced.

### C. MEASUREMENT RESULTS

Fig. 8b shows the resulting 2-D FL-MIMO-SAR image for the first experimental scenario. Thanks to the FL-MIMO-SAR, the target is resolved at the correct position with a

high angular resolution. However, the angular resolution refinement in this scenario is less than the one for targets far from the boresight, which is due to the DBS limitation. Moreover, a splitting in the mainlobe is observed, which can be attributed to the positioning error. This result is similar to the simulated scenario (see Fig. 6c).

Fig. 8d shows the resulting 2-D FL-MIMO-SAR image for the second experimental scenario. Both targets are resolved at the correct positions with a high angular resolution, thanks to the FL-MIMO-SAR. However, a relatively higher noise floor, as well as smearing effects, are observed in the image. This is due to the positioning error, which is slightly higher in this experiment because of the changing yaw of the radar (see the deviation in trajectory in Fig. 8c). This result is comparable with the simulated scenario (see Fig. 6f).

As for the third experimental scenario, Fig. 8f shows the resulting 2-D FL-MIMO-SAR image. Two of the three targets are correctly resolved at their respective positions with a high angular resolution (higher than the previous experimental scenarios because of the larger look angles). However, the third target (with a smaller radar cross-section) is shifted in range and angle. Moreover, a splitting of the mainlobe in the first two targets can be observed. This can be attributed to the high positioning error as well as the changing yaw of the radar (see the deviation in trajectory in Fig. 8e). Like in the previous two experimental scenarios, this result is comparable with the simulated scenario (see Fig. 6i).

Fig. 8h shows the resulting 2-D FL-MIMO-SAR image for the fourth experimental scenario. Here, the reconstructed image shows a signature that is close to that of the four-legged table. However, two legs from one side appear to reflect more echos than the other two legs. The reason for this can be the slight change in the yaw of the radar (see the deviation in trajectory in Fig. 8g). Moreover, and similarly to the previous cases, the smearing effects can be attributed to the positioning error.

Finally, Fig. 9b and Fig. 9d illustrate the geometry and resulting 2-D single snapshot image for the fifth experimental scenario, respectively. Thanks to the relatively large aperture (sparse MIMO array), the target is resolved at the correct position with a high angular resolution with a single snapshot. However, due to the sparsity in the MIMO array, grating lobes are formed in the imaged scene. Fig. 9e, which illustrates the resulting 2-D FL-sparseMIMO-SAR image in the fifth experimental scenario, shows significant suppression of the grating lobes. It can also be seen in Fig. 9e that the effective angular resolution in the radar boresight is higher than in Fig. 8b. This is due to the larger real MIMO aperture, which contributes to the angular resolution in the DBS-blind regions, see I. Furthermore, and thanks to the FL-sparseMIMO-SAR, shorter synthetic apertures can be utilized instead of longer ones, as the main contribution of the synthetic aperture is not the angular resolution refinement but rather the grating lobes suppression. From the relations illustrated in Fig. 3, and thanks to the Dec-BP approach, a relatively low number of snapshots is required to produce high-quality SAR images (with sufficiently suppressed grating lobes). This helps reduce the computational complexity as well as the positioning error artifacts of the SAR imaging system.

## VI. CONCLUSION

The applicability of the FL-MIMO-SAR imaging techniques for the applications of AMRs was evaluated and discussed. In addition, the geometry and the FMCW signal model for the FL-MIMO-SAR problem were presented. Aspects like model approximations, image reconstruction, complexity reduction, and left-right ambiguity for FL-MIMO-SAR imaging systems were addressed. Furthermore, the combination of FL-MIMO-SAR and sparse MIMO arrays (with large inter-element spacing) was analyzed.

To test and compare the usability of the FL-MIMO-SAR and the FL-sparseMIMO-SAR approaches for AMR applications, several scenarios were simulated and discussed. Simulation results showed significant improvement in the angular resolution of the FL-MIMO-SAR images. Moreover, the simulation results showed significant suppression of the grating lobes for the FL-sparseMIMO-SAR case. In addition, the simulation results were verified with four different experimental scenarios using an AMR with two different commercial radar sensors.

Looking at the experimental results, it is evident that the utilization of radar imaging systems with FL-MIMO-SAR capabilities will significantly enhance the quality of the produced radar images. However, this comes at the cost of high computational complexity due to the relatively large synthetic aperture needed for providing sufficient angular resolution refinement. Such a long synthetic aperture also makes the resulting SAR images susceptible to artifacts due to positioning errors.

On the other hand, the proposed FL-sparseMIMO-SAR helps to relax the requirements on the synthetic aperture length and solves the DBS-blind region problem, thanks to the larger real sparse MIMO array and the grating lobes suppression with the FL-SAR processing.

In summary, these results show a great potential for FL-sparseMIMO-SAR techniques to be employed in the applications of AMRs towards smarter factories and smarter warehouses.

That being said, the use of mmW radars with FL-MIMO-SAR and FL-sparseMIMO-SAR imaging techniques poses the following challenges:

- Knowledge of the platform motion parameters with sub-millimeter-level accuracy is required to produce well focused FL-MIMO-SAR images, especially for the case of faster vehicles.
- Non-cooperative moving targets (i.e., dynamic scenes) require tailored FL-MIMO-SAR solutions to produce well-focused FL-MIMO-SAR images.

Lastly, it is worth mentioning that the aforementioned challenges are currently being investigated and will be addressed in future works.

## REFERENCES


[1] C. Waldschmidt, J. Hasch, and W. Menzel, "Automotive radar—From first efforts to future systems," *IEEE J. Microw.*, vol. 1, no. 1, pp. 135–148, Jan. 2021, doi: 10.1109/JMW.2020.3033616.

[2] G. Brooker, J. Martinez, and R. Hennessey, "Millimetre wave radar imaging of mining vehicles," in *Proc. 7th Eur. Radar Conf.*, Paris, France, Sep. 2010, pp. 284–287.

[3] L. Nguyen and C. Le, "3D imaging for millimeter-wave forward-looking synthetic aperture radar (SAR)," *Proc. SPIE*. vol. 11411, pp. 83–94, May 2020.

[4] S. E. Navarro, S. Mühlbacher-Karrer, H. Alagi, H. Zangl, K. Koyama, B. Hein, C. Duriez, and J. R. Smith, "Proximity perception in human-centered robotics: A survey on sensing systems and applications," *IEEE Trans. Robot.*, vol. 38, no. 3, pp. 1599–1620, Jun. 2022, doi: 10.1109/TRO.2021.3111786.

[5] C. Stetco, B. Ubezio, S. Mühlbacher-Karrer, and H. Zangl, "Radar sensors in collaborative robotics: Fast simulation and experimental validation," in *Proc. IEEE Int. Conf. Robot. Autom. (ICRA)*, Paris, France, May 2020, pp. 10452–10458, doi: 10.1109/ICRA40945.2020.9197180.

[6] M. Harter, L. Zwirello, T. Schipper, A. Ziroff, and T. Zwick, "A novel sensing method for automatic guidance of trolley vehicles based on digital beamforming radar," in *Proc. IEEE Int. Conf. Wireless Inf. Technol. Syst. (ICWITS)*, Maui, HI, USA, Nov. 2012, pp. 1–4, doi: 10.1109/ICWITS.2012.6417832.

[7] M. G. Fernández, Y. Á. López, A. A. Arboleya, B. G. Valdés, Y. R. Vaqueiro, F. L.-H. Andrés, and A. P. García, "Synthetic aperture radar imaging system for landmine detection using a ground penetrating radar on board a unmanned aerial vehicle," *IEEE Access*, vol. 6, pp. 45100–45112, 2018, doi: 10.1109/ACCESS.2018.2863572.

[8] S. M. Patole, M. Torlak, D. Wang, and M. Ali, "Automotive radars: A review of signal processing techniques," *IEEE Signal Process. Mag.*, vol. 34, no. 2, pp. 22–35, Mar. 2017, doi: 10.1109/MSP.2016.2628914.

[9] C. Willey, "Synthetic aperture radars—A paradigm for technology evolution," *IEEE Trans. Aerosp. Electron. Syst.*, vol. AES-21, pp. 440–443, 1985.

[10] A. Moreira, P. Prats-Iraola, M. Younis, G. Krieger, I. Hajnsek, and K. P. Papathanassiou, "A tutorial on synthetic aperture radar," *IEEE Geosci. Remote Sens. Mag. Replaces Newsletter*, vol. 1, no. 1, pp. 6–43, Mar. 2013, doi: 10.1109/MGRS.2013.2248301.

[11] T. Espeter, I. Walterscheid, J. Klare, A. R. Brenner, and J. H. G. Ender, "Bistatic forward-looking SAR: Results of a spaceborne–airborne experiment," *IEEE Geosci. Remote Sens. Lett.*, vol. 8, no. 4, pp. 765–768, Jul. 2011, doi: 10.1109/LGRS.2011.2108635.

[12] X. Ren, J. Sun, and R. Yang, "A new three-dimensional imaging algorithm for airborne forward-looking SAR," *IEEE Geosci. Remote Sens. Lett.*, vol. 8, no. 1, pp. 153–157, Jan. 2011, doi: 10.1109/LGRS.2010.2055035.

[13] Y. Venot, M. Younis, and W. Wiesbeck, "Compact forward looking SAR using digital beamforming on receive only," in *Proc. EUSAR*, 2000, pp. 795–798.

[14] F. Witte, T. Sutor, and R. Scheunemann, "New sector imaging radar for enhanced vision: SIREV," *Proc. SPIE*, vol. 3364, pp. 115–122, Jun. 1998.

[15] S. Thomas, F. Witte, and A. Moreira, "New sector imaging radar for enhanced vision: SIREV," *Proc. SPIE*, vol. 3691, pp. 39–47, Jul. 1999.

[16] L. H. Nguyen, "Millimeter-wave forward-looking 3-D SAR imaging challenges," *Proc. SPIE*, vol. 10994, May 2019, pp. 145–151.

[17] A. Albaba, A. Sakhnini, H. Sahli, and A. Bourdoux, "Forward-looking MIMO-SAR for enhanced angular resolution," in *Proc. IEEE Radar Conf. (RadarConf)*, New York City, NY, USA, Mar. 2022, pp. 1–6, doi: 10.1109/RadarConf2248738.2022.9764255.

[18] R. Feger, A. Haderer, and A. Stelzer, "Experimental verification of a 77-GHz synthetic aperture radar system for automotive applications," in *Proc. IEEE MTT-S Int. Conf. Microw. Intell. Mobility (ICMIM)*, Nagoya, Japan, Mar. 2017, pp. 111–114, doi: 10.1109/ICMIM.2017.7918869.

[19] M. Hoffmann, T. Noegel, C. Schüßler, M. Vossiek, M. Schütz, and P. Gulden, "Filter-based segmentation of automotive SAR images," in *Proc. IEEE Radar Conf. (RadarConf)*, New York City, NY, USA, Mar. 2022, pp. 1–6, doi: 10.1109/RadarConf2248738.2022.9764276.

[20] M. Rizzi, M. Manzoni, S. Tebaldini, A. V. Monti–Guarnieri, C. M. Prati, D. Tagliaferri, M. Nicoli, I. Russo, C. Mazzucco, S. T. Alfageme, and U. Spagnolini, "Multi-beam automotive SAR imaging in urban scenarios," in *Proc. IEEE Radar Conf. (RadarConf)*, New York City, NY, USA, Mar. 2022, pp. 1–6, doi: 10.1109/RadarConf2248738.2022.9764331.

[21] H. Iqbal, A. Löffler, M. N. Mejdoub, and F. Gruson, "Realistic SAR implementation for automotive applications," in *Proc. 17th Eur. Radar Conf. (EuRAD)*, Utrecht, The Netherlands, Jan. 2021, pp. 306–309, doi: 10.1109/EuRAD48048.2021.00085.

[22] A. Albaba, S. Pollin, P. Wambacq, H. Sahli, and A. Bourdoux, "Theoretical angular resolution of forward-looking MIMO-SAR systems," in *Proc. 19th Eur. Radar Conf. (EuRAD)*, Milan, Italy, Sep. 2022, pp. 53–56, doi: 10.23919/EuRAD54643.2022.9924641.

[23] L. Lynch, T. Newe, J. Clifford, J. Coleman, J. Walsh, and D. Toal, "Automated ground vehicle (AGV) and sensor technologies—A review," in *Proc. 12th Int. Conf. Sens. Technol. (ICST)*, Dec. 2018, pp. 347–352.

[24] N. Sariff and N. Buniyamin, "An overview of autonomous mobile robot path planning algorithms," in *Proc. 4th Student Conf. Res. Develop.*, Jun. 2006, pp. 183–188.

[25] M. B. Alatise and G. P. Hancke, "A review on challenges of autonomous mobile robot and sensor fusion methods," *IEEE Access*, vol. 8, pp. 39830–39846, 2020, doi: 10.1109/ACCESS.2020.2975643.

[26] A. Hernández, C. Gómez, J. Crespo, and R. Barber, "Object detection applied to indoor environments for mobile robot navigation," *Sensors*, vol. 16, no. 8, p. 1180, Jul. 2016.

[27] A. Pandey, S. D. Pandey, and D. R. Parhi, "Mobile robot navigation and obstacle avoidance techniques: A review," *Int. Robot. Automat. J.*, vol. 2, no. 3, pp. 96–105, 2017.

[28] G. K. H. Pang and H. C. Shen, "Intelligent control of an autonomous mobile robot in a hazardous material spill accident—A blackboard structure approach," *Robot. Auto. Syst.*, vol. 6, no. 4, pp. 351–365, Oct. 1990.

[29] J. J. Leonard, H. F. Durrant-Whyte, and I. J. Cox, "Dynamic map building for an autonomous mobile robot," *Int. J. Robot. Res.*, vol. 11, no. 4, pp. 286–298, Aug. 1992.

[30] S. Li, J. Yan, and L. Li, "Automated guided vehicle: The direction of intelligent logistics," in *Proc. IEEE Int. Conf. Service Operations Logistics, Informat. (SOLI)*, Singapore, Jul. 2018, pp. 250–255, doi: 10.1109/SOLI.2018.8476726.

[31] T. R. Anusha, S. S. Kumar, and S. Panday, "ROS based obstacle detection robot using ultrasonic sensor and FMCW RADAR," in *Proc. 3rd Int. Conf. Electron. Sustain. Commun. Syst. (ICESC)*, Coimbatore, India, Aug. 2022, pp. 372–378, doi: 10.1109/ICESC54411.2022.9885346.

[32] W. Chen, F. Zhang, T. Gu, K. Zhou, Z. Huo, and D. Zhang, "Constructing floor plan through smoke using ultra wideband radar," *Proc. ACM Interact., Mobile, Wearable Ubiquitous Technol.*, vol. 5, 2021, pp. 1–29.

[33] Z. Jiang, J. Wang, Q. Song, and Z. Zhou, "Negative obstacle sensing based on real data of ultra-wideband SAR," in *Proc. IET Int. Radar Conf.*, Oct. 2015, pp. 1–5.

[34] P. Tripicchio, M. Unetti, S. D'Avella, A. Buffi, A. Motroni, F. Bernardini, and P. Nepa, "A synthetic aperture UHF RFID localization method by phase unwrapping and hyperbolic intersection," *IEEE Trans. Autom. Sci. Eng.*, vol. 19, no. 2, pp. 933–945, Apr. 2022, doi: 10.1109/TASE.2021.3057433.

[35] S. Gishkori, L. Daniel, M. Gashinova, and B. Mulgrew, "Imaging for a forward scanning automotive synthetic aperture radar," *IEEE Trans. Aerosp. Electron. Syst.*, vol. 55, no. 3, pp. 1420–1434, Jun. 2019, doi: 10.1109/TAES.2018.2871436.

[36] S. Gishkori, L. Daniel, M. Gashinova, and B. Mulgrew, "Imaging moving targets for a forward scanning SAR without radar motion compensation," *Signal Process.*, vol. 185, Aug. 2021, Art. no. 108110.

[37] S. L. Cassidy, S. Pooni, M. Cherniakov, E. G. Hoare, and M. S. Gashinova, "High-resolution automotive imaging using MIMO radar and Doppler beam sharpening," *IEEE Trans. Aerosp. Electron. Syst.*, vol. 59, no. 2, pp. 1495–1505, Apr. 2023, doi: 10.1109/TAES.2022.3203953.

[38] M. Manzoni, S. Tebaldini, A. V. Monti-Guarnieri, C. M. Prati, D. Tagliaferri, M. Nicoli, U. Spagnolini, I. Russo, and C. Mazzucco, "Automotive SAR imaging: Potentials, challenges, and performances," *Int. J. Microw. Wireless Technol.*, early access, pp. 1–10, Apr. 2023.

[39] M. Marco, S. Tebaldini, A. V. Monti-Guarnieri, C. M. Prati, and I. Russo, "A comparison of processing schemes for automotive MIMO SAR imaging," *Remote Sens.*, vol. 14, no. 19, p. 4696, 2022.

[40] M. Farhadi, R. Feger, J. Fink, T. Wagner, and A. Stelzer, "Automotive synthetic aperture radar imaging using TDM-MIMO," in *Proc. IEEE Radar Conf. (RadarConf)*, Atlanta, GA, USA, May 2021, pp. 1–6, doi: 10.1109/RadarConf2147009.2021.9455230.

[41] A. Laribi, M. Hahn, J. Dickmann, and C. Waldschmidt, "Performance investigation of automotive SAR imaging," in *Proc. IEEE MTT-S Int. Conf. Microw. for Intell. Mobility (ICMIM)*, Munich, Germany, Apr. 2018, pp. 1–4, doi: 10.1109/ICMIM.2018.8443554.
[42] D. Tagliaferri, M. Rizzi, M. Nicoli, S. Tebaldini, I. Russo, A. V. Monti-Guarnieri, C. M. Prati, and U. Spagnolini, "Navigation-aided automotive SAR for high-resolution imaging of driving environments," *IEEE Access*, vol. 9, pp. 35599–35615, 2021, doi: 10.1109/ACCESS.2021.3062084.
[43] V. C. Koo, T. S. Lim, and H. T. Chuah, "A comparison of autofocus algorithms for SAR imagery," *PIERS Online*, vol. 1, no. 1, pp. 16–19, 2005.
[44] M. G. Polisano, M. Manzoni, S. Tebaldini, A. Monti-Guarnieri, C. M. Prati, and I. Russo, "Very high resolution automotive SAR imaging from burst data," *Remote Sens.*, vol. 15, no. 3, p. 845, Feb. 2023.
[45] J. Högbom, "Aperture synthesis with a non-regular distribution of interferometer baselines," *Astron. Astrophys. Suppl.*, vol. 15, p. 417, Jun. 1974.
[46] M. Cheney and B. Borden, *Fundamentals of Radar Imaging*. Philadelphia, PA, USA: SIAM, 2009.
[47] J. K. Jao, "Theory of synthetic aperture radar imaging of a moving target," *IEEE Trans. Geosci. Remote Sens.*, vol. 39, no. 9, pp. 1984–1992, Sep. 2001, doi: 10.1109/36.951089.
[48] M. Farhadi, R. Feger, J. Fink, T. Wagner, M. Gonser, J. Hasch, and A. Stelzer, "Phase error estimation for automotive SAR," in *IEEE MTT-S Int. Microw. Symp. Dig.*, Linz, Austria, Nov. 2020, pp. 1–4, doi: 10.1109/ICMIM48759.2020.9298998.
[49] L. Gorham and L. Moore, "SAR image formation toolbox for MATLAB," *Proc. SPIE*, vol. 7699, pp. 46–58, Apr. 2010.
[50] L. M. H. Ulander, H. Hellsten, and G. Stenstrom, "Synthetic-aperture radar processing using fast factorized back-projection," *IEEE Trans. Aerosp. Electron. Syst.*, vol. 39, no. 3, pp. 760–776, Jul. 2003, doi: 10.1109/TAES.2003.1238734.

**ADNAN ALBABA** received the B.Sc. degree in biomedical engineering from the Jordan University of Science and Technology (JUST), Irbid, Jordan, in 2016, and the M.Sc. degree in embedded systems from Uppsala Universitet (UU), Uppsala, Sweden, in 2019. He is currently pursuing the Ph.D. degree in engineering sciences with Vrije Universiteit Brussel (VUB), Brussels, Belgium, in collaboration with the Interuniversity Microelectronics Centre (IMEC), Leuven, Belgium. His current research interests include radar systems and signal processing, radar imaging, synthetic aperture radar, and biomedical systems and signal processing.

**MARC BAUDUIN** received the M.Sc. degree in electrical engineering from Universite Libre de Bruxelles (ULB), Belgium, in 2012, and the Ph.D. degree in engineering science from the Joint Optics, Photonics, Electromagnetism, Radio-Communications, and Acoustics (OPERA) and Laboratoire d'Information Quantique (LIQ) Department, ULB, in 2016. In 2016, he joined IMEC, where he is currently a Researcher with the Advanced RF Group. His current research interests include millimeter-wave MIMO radar signal processing, waveform design, automotive, and healthcare radar applications.

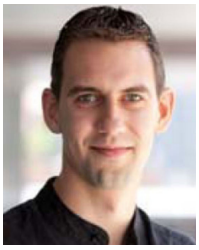

**TIM VERBELEN** received the M.Sc. and Ph.D. degrees in computer science engineering from Ghent University, Ghent, Belgium, in 2009 and 2013, respectively. Since then, he has been a Senior Researcher with Ghent University and IMEC, Leuven, Belgium. His current research interests include perception and control for autonomous systems using deep learning techniques and high-dimensional sensors, such as cameras, lidar, and radar. In particular, he is active in the domain of representation learning and reinforcement learning, inspired by cognitive neuroscience theories, such as active inference.

**HICHEM SAHLI** received the degree in mathematics and computer science, the D.E.A. degree in computer vision, and the Ph.D. degree in computer sciences from Télécom Physique Strasbourg, France. Since 2000, he has been a Professor with the Department of Electronics and Informatics (ETRO) and a Scientist with the Interuniversity Microelectronics Centre (IMEC). He coordinates the Audio-Visual Signal Processing Laboratory (AVSP) within ETRO. AVSP researches applied and theoretical problems related to machine learning, signal and image processing, and computer vision. The group explores and capitalizes on the correlation between speech and video data for computational intelligence where efficient numerical methods of computational engineering are combined with the problems of information processing.

**ANDRÉ BOURDOUX** (Senior Member, IEEE) received the M.Sc. degree in electrical engineering from Université Catholique de Louvain, Belgium, in 1982. He joined the Interuniversity Microelectronics Centre (IMEC), in 1998, where he is currently the Principal Member of Technical Staff with the Advanced RF Research Group. He is also a system-level and signal-processing expert for both the mm-wave wireless communications and radar teams. He has more than 15 years of research experience in radar systems and 15 years of research experience in broadband wireless communications. He holds several patents in these fields. He is the author and coauthor of more than 180 publications in books and peer-reviewed journals and conferences. His current research interests include advanced architectures, signal processing and machine learning for the wireless physical layer, and high-resolution 3D/4D radars.